

# Computational Aeroelastic Analysis of the Ares I Crew Launch Vehicle During Ascent

Robert E. Bartels,\* Pawel Chwalowski,† Steven J. Massey,† and Jennifer Heeg\*

NASA Langley Research Center, Hampton, Virginia 23681

and

Raymond E. Mineck‡

ATK Aerospace Company, Hampton, Virginia 23681

DOI: 10.2514/1.A32127

Static and dynamic aeroelastic analyses have been performed for the Ares I crew launch vehicle during atmospheric ascent. It is shown that, through the transonic speed range, there is a rapid change in the static aeroelastic center-of-pressure increment with increasing Mach number. The greatest sensitivity to grid resolution is observed through the transonic range. Dynamic aeroelastic analyses are also performed to assess the aeroelastic stability of the launch vehicle. Flexible dynamic linearized quasi-steady analyses using steady rigid line loads are compared with fully coupled aeroelastic time-marching computational fluid dynamic analyses. There are significant differences between the methods through the transonic Mach number range. The largest difference is at Mach 1. At that Mach number, the linearized quasi-steady method produces strong damping in modes 1 and 2. The unsteady computational aeroelastic method indicates that the first mode is significantly undamped, while mode 2 is strongly damped. The cause of the disparity in damping between modes 1 and 2 is also investigated. A vehicle with no protuberances other than rings produced damping values in modes 1 and 2 that were nearly identical. It is shown that the disparity in damping of modes one and two is due to asymmetric placement of protuberances around the vehicle circumference.

## Nomenclature

|                    |  |
|--------------------|--|
| $[B_{\text{cfd}}]$ | = projection matrix, structure to computational fluid dynamics surface nodes           |
| $[B_{ll}]$         | = projection matrix, structure to section loads analysis points                        |
| $\{C\}$            | = vector of nondimensional $x$ , $y$ , and $z$ -direction line loads                   |
| $C_m$              | = pitch moment coefficient about gimbal point  |
| $C_z$              | = force coefficient in $z$ direction   |
| $c_a$              | = aerodynamic damping, $\text{lb} \cdot \text{s}/\text{in}$ .                          |
| $c_{\text{cr}}$    | = critical structural damping ( $2M_s\omega$ ), $\text{lb} \cdot \text{s}/\text{in}$ . |
| $c_s$              | = structural damping, $\text{lb} \cdot \text{s}/\text{in}$ .                           |
| $D_{\text{ref}}$   | = reference diameter, in.  |
| $\{f\}$            | = vector of forces at computational fluid dynamics node points, lb                     |
| $\{G\}$            | = generalized force vector   |
| $\{g\}$            | = generalized variable   |
| $\{g_d\}$          | = dynamic component of generalized variable  |
| $\{g_s\}$          | = static (mean) component of generalized variable                                      |
| $\{I\}$            | = identity matrix  |
| $N_{\text{cfd}}$   | = number of computational fluid dynamics surface nodes                                 |
| $N_{ll}$           | = number of section nodes  |
| $N_s$              | = number of centerline structure nodes   |
| $q_{\text{nom}}$   | = freestream dynamic pressure at nominal ascent, psi                                   |
| $q_{\infty}$       | = freestream dynamic pressure, psi   |

|                       |  |
|-----------------------|--|
| $S_{\text{ref}}$      | = reference area, $\text{in}^2$  |
| $[T_y]$               | = $y$ transformation matrix  |
| $[T_z]$               | = $z$ transformation matrix  |
| $U_{\infty}$          | = freestream velocity, $\text{in}/\text{s}$ .                          |
| $\alpha$              | = vehicle angle of attack, rad   |
| $\{\alpha_i\}$        | = vector of local angles of attack, rad                                |
| $\beta$               | = vehicle angle of sideslip, rad                                       |
| $\{\beta_i\}$         | = vector of local angles of sideslip, rad                              |
| $[\Delta]$            | = structural and aerodynamic damping matrix                            |
| $\{\delta\}$          | = total displacement vector, in.                                       |
| $\Delta x$            | = $x$ distance between section load points, in.                        |
| $\{\delta_d\}$        | = dynamic aeroelastic displacement vector, in.                         |
| $\{\delta_s\}$        | = static aeroelastic displacement vector, in.                          |
| $\zeta_a$             | = aerodynamic damping ratio ( $c_a/c_{\text{cr}}$ )                    |
| $\zeta_s$             | = structural damping ratio ( $c_s/c_{\text{cr}}$ )                     |
| $\rho_{\infty}$       | = freestream density, $\text{slug} \cdot \text{in}/\text{in}^3$        |
| $\tau$                | = pseudotime   |
| $[\phi]$              | = matrix of eigenvectors of structural dynamics equations              |
| $[\Phi_{\text{cfd}}]$ | = modal vectors projected to computational fluid dynamics surface mesh |
| $[\Phi_{ll}]$         | = modal vectors projected to section loads analysis points             |
| $\{\chi\}$            | = state variable vector  |
| $[\Omega]$            | = structural and aerodynamic stiffness matrix                          |
| $\omega$              | = frequency of vehicle structural modes, $\text{rad}/\text{s}$ .       |

## I. Introduction

THE aeroelastic stability of launch vehicles has been a concern since at least the early development of Saturn I [1,2]. Furthermore, vehicles with a hammerhead configuration, having an upper stage diameter larger than the first stage, have been shown to have an additional potential for aeroelastic instability [3,4]. One of the notable features of the Ares I is the use of a five-segment solid rocket booster (SRB) as a first stage with a larger diameter upper stage. The two stages are connected by an aft-facing frustum. Along with the usual geometric complexity associated with a major launch vehicle, this hammerhead configuration is a challenge to model with computational fluid dynamics (CFD) because of the potential the configuration has of producing flowfield separation from the frustum. Combined with shock-induced flow separation over the

Presented as Paper 2010-4374 at the 28th AIAA Applied Aerodynamics Conference, Chicago, IL, 28 June–1 July 2010; received 24 May 2011; revision received 7 September 2011; accepted for publication 13 September 2011. This material is declared a work of the U.S. Government and is not subject to copyright protection in the United States. Copies of this paper may be made for personal or internal use, on condition that the copier pay the \$10.00 per-copy fee to the Copyright Clearance Center, Inc., 222 Rosewood Drive, Danvers, MA 01923; include the code 0022-4650/12 and \$10.00 in correspondence with the CCC.

\*Senior Aerospace Engineer, Aeroelasticity Branch, Mail Stop 340. Senior Member AIAA.

†Aerospace Engineer, Aeroelasticity Branch, Mail Stop 340. Senior Member AIAA.

‡Space Division. Senior Member AIAA.

upper stage, flow separation at the frustum can significantly influence overall vehicle aerodynamics [3–5]. In addition, the first-stage SRB aftskirt adds an additional mechanism for dynamic aeroelastic instability due to the disturbance time lag between the upper stage, the frustum, and the aftskirt [4]. These features of the Ares vehicle have motivated the widespread use of high-fidelity Reynolds-averaged Navier–Stokes (RANS) analyses, including a modeling of both static and dynamic fluid/structure interaction.

To the authors' knowledge, the first attempts to provide unsteady CFD in flexible launch vehicle analysis were performed by Azevedo [6]. This analysis tended to confirm the destabilizing effects predicted by the earlier analyses of Ericsson [4]. The use of CFD in the analysis of launch vehicles has expanded over the last several decades [6–12]. For current and future launch vehicles, it can be expected that CFD will be an integral part of the design from the conceptual stage. Vehicles will very likely be designed with a smaller proportion of aerodynamic data derived from wind-tunnel testing and a larger proportion due to CFD [13]. This approach to launch vehicle design poses both exciting possibilities in the extent to which the aerodynamics and flowfield physics of a launch vehicle can be understood as well as challenges in validating methodologies for the highly complex flowfield about a launch vehicle.

At the same time, the common method to simulate flexible launch vehicle dynamics is the quasi-steady method of line loads. This approach models the displacement and inertial, elastic, and aerodynamic forces by a distribution along the vehicle centerline axis. The aerodynamic forcing is usually derived from steady state rigid aerodynamics, either from a wind-tunnel test, slender body theory, or CFD. This approach is based upon the assumption that, unlike lifting surfaces, the loading of a slender flexible launch vehicle can be approximated by a series of sectional loads each independently computed from rigid sectional aerodynamics. Combined with a model of vehicle buffeting or gust loading, this method provides a rapid simulation tool for the vehicle response dynamics during ascent. The origin of the method dates at least to Saturn I analyses [2,14], and the aerodynamic modeling of section loads dates even earlier to slender body theory [15]. The vehicle structure typically is modeled as a simple beam [3,4,16–18]. This approach has been applied to launch vehicles [3,4,16,19], tactical weapons [17], and hypersonic atmospheric reentry vehicles [18].

The limitation of the quasi-steady aeroelastic method of line loads is that it does not represent a true aeroelastic interaction of the vehicle in flight. The use of rigid steady aerodynamics assumes that each station along the body is influenced only by local angle of attack and not by flexibility-induced downwash from upstream or downstream aerodynamic response to flexibility. Simulating the unsteady flexible response by a quasi-steady method is further removed from reality, unless a correction is included to account for the time lag associated with flow separation. Ericsson has developed a quasi-steady analytical method of sectional loads using steady-state wind-tunnel data that incorporate corrections to the aerodynamic damping based on an assumed disturbance time lag [4]. This lag is due to the time required for boundary-layer separation to grow in response to vehicle motion in an unsteady flowfield compared with a steady flowfield. The analytical/empirical approach of Ericsson and Pavish does provide an initial rapid approximation to the phase shift [3], and thus the destabilizing effect of unsteady aerodynamics. However, it is only approximate and somewhat heuristic. Nevertheless, it can provide an initial assessment of aeroelastic stability.

In the present work, we have initiated unsteady aeroelastic CFD early in the conceptual design stage. The goal is to provide an accurate analysis of vehicle aeroelastic stability early in the vehicle design. Computational aeroelastic (CAE) analyses have been performed for the Ares I crew launch vehicle in two areas. The first is an understanding of the influence of flexibility on static loading and controllability. To quantify the static influence of flexibility, aeroelastic center-of-pressure increments are obtained over the nominal vehicle ascent trajectory. This paper will compare results derived by a fully coupled fluid/structure CAE analysis method with the quasi-steady method of line loads. A second area is an assessment of the dynamic aeroelastic stability of the launch vehicle. Design practice

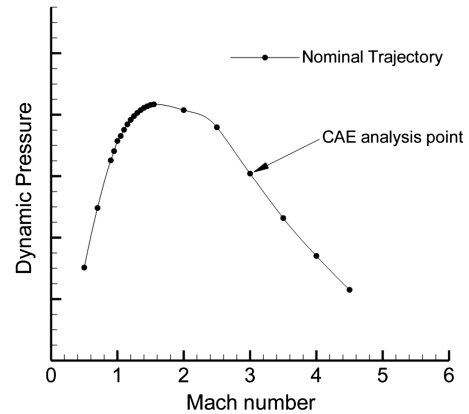


Fig. 1 Trajectory and analysis points.

requires that a launch vehicle be free of flutter beyond 1.32 times the nominal ascent dynamic pressure [20]. If analysis shows dynamic aeroelastic instability within this range, aeroelastic wind-tunnel testing is required, and ultimately a flutter clearance of the vehicle. In response to this requirement, a complete range of analyses has been conducted. Aeroelastic stability will be presented using an eigenvalue analysis of the quasi-steady equations and using a time-marching dynamic aeroelastic CFD analysis. The present results all assume that there are no rigid body rotational accelerations and considers only the influence of transverse flexibility.

The outer mold line (OML) used in the present paper is the Ares I A105. Figure 1 shows the lunar ascent trajectory with dynamic pressure in terms of vehicle Mach number. The symbols represent the complete set of analysis points. Static and dynamic aeroelastic results using an unstructured node based RANS CAE code will be presented at several of these conditions to highlight key features of the vehicle aeroelastic behavior.

## II. Methods of Analysis

### A. Fully Unstructured Navier–Stokes Three-Dimensional Aeroelastic Solver

The Navier–Stokes code used in this study is the fully unstructured Navier–Stokes three-dimensional (FUN3D). The FUN3D flow solver is a finite volume unstructured CFD code for either compressible or incompressible flows [21,22]. Flow variables are stored at the vertices of the mesh. In the present study, the RANS solver and the loosely coupled Spalart–Allmaras turbulence model are used on a tetrahedral grid [23]. FUN3D employs an implicit upwind algorithm. The low dissipation flux splitting scheme for the inviscid flux construction and the blended van Leer flux limiter were used. For tetrahedral meshes, the full viscous fluxes are made discrete by using a finite volume formulation in which the required velocity gradients on the dual faces are computed using the Green–Gauss theorem [24]. This approach is equivalent to a Galerkin-type approximation. The solution at each time step is updated with a backward Euler time differencing scheme and the use of local time stepping. At each time step, the linear system of equations is approximately solved either with a multicolor point-implicit procedure or an implicit-line relaxation scheme [25]. Domain decomposition exploits the distributed high-performance computing architectures that are necessary for the grid sizes used in the present study.

For a moving mesh, the conservation equations are written in the arbitrary Lagrange–Euler formulation [26]. The mesh deformation is accomplished by treating the mesh as linear elasticity problem [27]. Element stiffnesses vary in inverse proportion to distance from a solid boundary. The displacements are computed from the finite volume formulation of the elasticity equations using the generalized minimum residual algorithm [26,28].

The present aeroelastic analysis uses a modal decomposition of the structural model. An orthogonal transformation of the finite element equations provides the eigenvalues and eigenvectors from which the

mode shapes and structural frequencies are derived. The transformed equations of elastic structural dynamics are

$$[I]\{\ddot{g}\} + [2\zeta_s\omega]\{\dot{g}\} + [\omega^2]\{g\} = q_\infty[\Phi_{\text{cfd}}]^T\{f\} \quad (1)$$

where

$$[\Phi_{\text{cfd}}] = [B_{\text{cfd}}][\phi] \quad (2)$$

and  $[B_{\text{cfd}}]$  is a  $3N_{\text{cfd}} \times 3N_s$  projection matrix relating structural centerline nodes to CFD surface nodes,  $[\phi]$  is a  $3N_s \times N_{\text{modes}}$  matrix of eigenvectors, and  $[\Phi_{\text{cfd}}]$  is a  $3N_{\text{cfd}} \times N_{\text{modes}}$  matrix of mode shapes projected to the CFD surface nodes.

### B. Static and Dynamic Aeroelastic Analysis Based on Section Loads

The present paper formulates a flexibilized rigid integrated line loads (FRILLS) method that uses integrated surface pressures derived from rigid steady CFD coupled with a vehicle structural dynamics model that has been reduced to the vehicle centerline. Unlike previous quasi-steady sectional loading methods based on beam theory, the present method uses a Guyan reduction to the centerline of the full stack vehicle finite element model. This approach is fully compatible with the Guyan reduction also used in the FUN3D aeroelastic solutions. Compatibility of the two solution methods allows mixing models to perform rapid parametric studies of the influence of aeroelasticity on the system. By comparing FUN3D CAE with FRILLS solutions, we have a way to assess the effect of a full aeroelastic interaction on the static and dynamic responses of the vehicle.

The quasi-steady method of line loads simplifies the aeroelastic response of the vehicle to displacements along the vehicle centerline axis and applies elastic, inertial, and aerodynamic forces at uniformly distributed points along that axis. Figure 2 shows the vehicle with the coordinate system superimposed. The vehicle is partitioned into  $N_{ll}$  stations. Displacements at each station can be written as a sum of static aeroelastic and dynamic aeroelastic displacements. The displacement is defined as  $\{\delta\} = (\delta_{1x}, \delta_{1y}, \delta_{1z}, \dots, \delta_{N_{ll}x}, \delta_{N_{ll}y}, \delta_{N_{ll}z})^T$ , where

$$\{\delta\} = \{\delta_s\} + \{\delta_d\}, \quad \{\delta_s\} = f(x), \quad \{\delta_d\} = f(x, t) \quad (3)$$

$\{\delta_s\}$  and  $\{\delta_d\}$  are the static and dynamic aeroelastic centerline displacements, respectively, as functions of the vehicle  $x$  station and time  $t$ . The material derivative yields an approximation for the local angles of attack and side slip:

$$\begin{aligned} \{\alpha_l\} &\approx \alpha + \frac{1}{U_\infty}[T_z] \left\{ \frac{\partial\{\delta_d\}}{\partial t} + U_\infty \left( \frac{\partial\{\delta_s\}}{\partial x} + \frac{\partial\{\delta_d\}}{\partial x} \right) \right\} \\ \{\beta_l\} &\approx \beta + \frac{1}{U_\infty}[T_y] \left\{ \frac{\partial\{\delta_d\}}{\partial t} + U_\infty \left( \frac{\partial\{\delta_s\}}{\partial x} + \frac{\partial\{\delta_d\}}{\partial x} \right) \right\} \end{aligned} \quad (4)$$

where matrices  $[T_y]$  and  $[T_z]$  are defined in the Appendix.

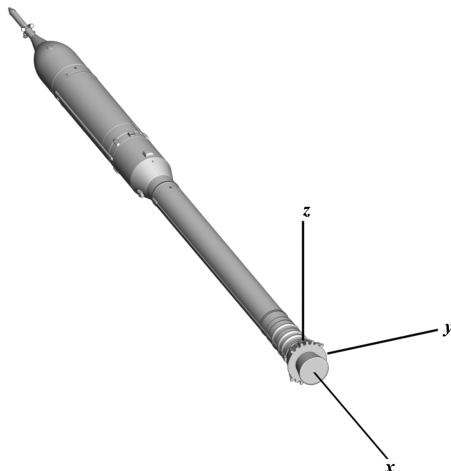


Fig. 2 Coordinate system with origin at SRB gimbal point.

The mode shapes from the finite element model are projected to the analysis points along the vehicle. The projection can be written as

$$[\Phi_{ll}] = [B_{ll}][\phi] \quad (5)$$

where  $[B_{ll}]$  is an  $3N_{ll} \times 3N_s$  projection matrix relating structural and sectional centerline nodes, and  $[\Phi_{ll}]$  is a  $3N_{ll} \times N_{\text{modes}}$  matrix of mode shapes projected to the sectional centerline nodes. The matrices  $[B_{ll}]$  and  $[B_{\text{cfd}}]$  use the same method of projection to ensure consistency of the sectional load and FUN3D CAE results. The modal transformation yields

$$\{g\} = \{g_s\} + \{g_d\} = [\phi]^T[B_{ll}]^T(\{\delta_s\} + \{\delta_d\}) \quad (6)$$

where  $g_s$  is the generalized variable due to static loading, and  $g_d$  is the generalized variable responding to vehicle dynamic forcing. The generalized forcing due to aerodynamics can be written in terms of the  $3N_{ll}$ -dimensional section loading  $\{C\}$

$$\{G\} = \frac{q_\infty S_{\text{ref}} \Delta x}{D_{\text{ref}}} [\phi]^T [B_{ll}]^T \{C\} \quad (7)$$

where

$$\{C\} = \{C_{1x} \ C_{1y} \ C_{1z} \ \dots \ C_{N_{ll}x} \ C_{N_{ll}y} \ C_{N_{ll}z}\}^T \quad (8)$$

The line loads at each body station  $n$  of  $C_{nx}$ ,  $C_{ny}$ , and  $C_{nz}$  are functions of Mach number, angle of attack, and angle of side slip.

The line loads are integrated from vehicle surface pressure coefficients that were computed using the FUN3D code. The integration is accomplished using a discrete data transfer algorithm developed by Samareh [29]. The approach is based on that of Farhat et al. [30], which is a variation of the inverse isoparametric method (IIM). The further modified IIM algorithm of Samareh [29] maintains conservation of momentum and energy between separate meshes having dissimilar mesh spacing by an integration of loads on the source mesh and injection of the force vectors to the target mesh. Having transferred discrete loads from the unstructured CFD mesh to the sectional mesh, the nodal loads are integrated into sectional loads. The sectional loads are assembled by computing CFD solutions for the rigid vehicle at each Mach number at a series of angles of attack and sideslip.

Computation of the static aeroelastic solution using line loads can be performed by treating the structural dynamics in pseudotime  $\tau$ . The generalized aerodynamic forcing is updated at each iteration using the current  $\alpha_l$  and  $\beta_l$ . The static structural modal damping and dilation of time step are set to optimize convergence to a static solution. Once a converged static aeroelastic solution is obtained, the time-accurate dynamic response of the vehicle can be computed by linearizing the line loads around the local static  $\alpha_l$ ,  $\beta_l$ , and static generalized force. The linearized equation can be written as

$$[I]\{\ddot{g}_d\} + [\Delta]\{\dot{g}_d\} + [\Omega]\{g_d\} = 0 \quad (9)$$

where

$$[\Omega] = [\omega^2] - \rho_\infty U_\infty^2 [Q_k], \quad [\Delta] = [2\zeta_{sd}\omega] - \rho_\infty U_\infty [Q_\zeta] \quad (10)$$

$$[Q_\zeta] = \frac{S_{\text{ref}} \Delta x}{2D_{\text{ref}}} [\phi]^T [B_{ll}]^T \left\{ \frac{\partial\{C\}}{\partial\alpha} [\hat{S}][T_z] + \frac{\partial\{C\}}{\partial\beta} [\hat{S}][T_y] \right\} [B_{ll}][\phi] \quad (11)$$

and

$$[Q_k] = \frac{S_{\text{ref}} \Delta x}{2D_{\text{ref}}} [\phi]^T [B_{ll}]^T \left\{ \frac{\partial\{C\}}{\partial\alpha} [\hat{S}][T_z] + \frac{\partial\{C\}}{\partial\beta} [\hat{S}][T_y] \right\} [B_{ll}] \left[ \frac{\partial\phi}{\partial x} \right] \quad (12)$$

The  $3N_{ll} \times 3N_{ll}$  square matrices  $\partial\{C\}/\partial\alpha$  and  $\partial\{C\}/\partial\beta$  are constructed, placing along the diagonals the derivative of  $\{C\}$ . The derivatives with respect to  $\alpha$  and  $\beta$  are computed from a spline fit of

the aerodynamic section loadings. The matrices  $[\hat{S}]$ ,  $[T_y]$ , and  $[T_x]$  are defined in the Appendix. Equation (9) can be written in state space as

$$\{\dot{\chi}\} = [A]\{\chi\}, \quad \{\chi\} = \{g_d, \dot{g}_d\}^T \quad (13)$$

where

$$[A] = \begin{bmatrix} 0 & I \\ -\Omega & -\Delta \end{bmatrix} \quad (14)$$

The eigenanalysis of this system provides aeroelastic damping and frequency at a given flight condition.

### III. Models

#### A. Computational Fluid Dynamics Mesh

The unstructured tetrahedral grids used in this study were created using VGRID [31]. Four grids were developed and designated the extra coarse, coarse, baseline, and fine [32]. The extra coarse grid had 10 million nodes, the coarse grid had 19 million nodes, the baseline had 41 million nodes, and the fine grid had 83 million nodes. Clustering of grid points near protuberances, rings, and other geometric discontinuities was used to aid in resolving flow features. The refinement of successive grid levels was accomplished by doubling the number of surface nodes uniformly everywhere. The boundary-layer normal spacing was kept unchanged from one grid level to the next. Refinement studies using the finer grids were done for a few critical cases in the transonic Mach number range. Additional details about the grid development and refinement studies are discussed in a separate paper [32]. Because of the computational expense, the coarse level grid was used for most of the computations performed here.

#### B. Structural Model

The structural models are MSC.Nastran<sup>TM</sup> finite element models. Two Ares I models were used in the present analysis. Each model includes a finite element modeling of the first stage, the first-stage solid propellant, the second stage including liquid fuel and oxidizer masses, the crew exploration vehicle, and the launch abort system. The baseline Ares I model is designated the Ares I Integrated Model 1 (AIIM1). The second Ares I model is otherwise identical but includes an upper stage thrust oscillation isolator (AIIM1-TOI).

The Orion configuration used here is the liftoff configuration for the lunar mission. The Orion structural data consist of a stiffness matrix produced by Craig-Bampton analysis, retaining information only along the centerline and an interface circumference where the Orion connects to the upper stage. The upper stage configuration contains fluid elements, pressure stiffening, and temperature effects of the J-2X engine. The first-stage solid propellant is modeled as four concentrated masses. Because the first-stage propellant mass changes during atmospheric ascent, there is a continuous change in the stiffness and mass properties of the first stage. First-stage

propellant mass data were defined at a rather coarse spacing of ascent times, namely, at 0, 20, 40, 50, 60, 80, 100, and 115 s. The lunar mission trajectory data, including total vehicle mass, are defined significantly more finely. To apply propellant mass data in a consistent manner, the coarsely spaced propellant data were interpolated to the present analysis points by matching total mass with the trajectory vehicle mass.

An additional structural model is used here that incorporates a thrust oscillation isolator (AIIM1-TOI). The AIIM1-TOI model is a dual-plane isolation system intended to isolate the upper stage from first-stage thrust oscillation. The isolator mechanism was modeled by a circumferential ring of springs at the interface between the Orion and the upper stage, and a circumferential ring of spring elements and mass elements at the interface between the upper stage and the first stage. In all other respects, the AIIM1-TOI model is identical to the baseline structural model.

The entire structural model was reduced to 51 points along the vehicle centerline by a Guyan reduction. This reduction produced both translational and rotational modal deflections. Mode shapes having only axial or rotational deflections were discarded. Likewise, rigid body modes were also not included in the present analysis. The remaining modes were ranked by the moduli of the mode shape amplitude, and the top 37 flexible modes were retained. The translational deflections of the remaining modes were projected with a third-order spline fit to the CFD surface mesh points.

The liftoff frequencies of the retained modes span from 1.0 to 39 Hz. As SRB propellant is burned, vehicle mass decreases and the frequencies of propellant related modes change. The first bending mode frequencies increase by 15–25% over the ascent. Mode switching also occurs. An analysis of the modal frequencies through the entire ascent showed that, by including 37 modes, none of the important modes were lost to modal switching. Because of the additional springs located in the upper stage, the first mode frequencies of the AIIM1-TOI model are slightly lower than that of the AIIM1 model. The orientation of the  $x$ -,  $y$ -, and  $z$ -coordinate system with respect to the vehicle is shown in Fig. 2. The transverse  $y$  and  $z$  components of the coupled first two modes of the AIIM1 model are shown in Fig. 3. These modes have an identical frequency but orthogonal modal amplitudes. Many modes over the entire frequency range exhibit similar pairing.

The finite element structural models per se do not include information about the structural damping. The preliminary design of the Ares I has relied on historical data to provide estimates. Hanson and Doggett measured the Saturn I wind-tunnel model structural damping ratio ( $\zeta_s = c_s/c_{cr}$ ) in the range of 0.007 to 0.018 [15,33]. Subsequent models and full-scale estimates of the Apollo/Saturn structural damping ratio were put at 0.012 to 0.022 [1]. In the present aeroelastic analysis, an assumed nominal structural damping ratio value of 0.005 is used for all modes throughout the ascent. This value of the damping ratio is consistent with the conservative value of structural damping of the first bending mode assumed in previous studies [4].

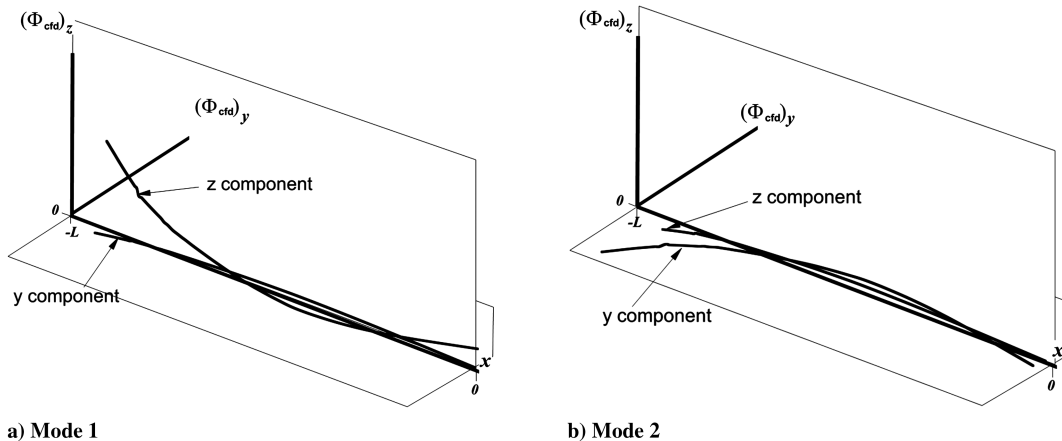


Fig. 3 Ares I first bending modes.  $x$ -coordinate origin at gimbal point.

### IV. Results

#### A. Aeroelastic Analysis Process

Aeroelastic analysis using the FUN3D software is performed as a multistep process. From a steady-state rigid solution, a static aeroelastic computation provides a steady-state flexible vehicle solution. Starting from a static aeroelastic solution, the dynamic solution is initiated by perturbing each mode with an initial generalized velocity. In this analysis, the time step for dynamic analyses has been selected to provide 700–1000 time steps per cycle of the first flexible mode and approximately 30 time steps per cycle for the highest frequency mode. The number of subiterations is set to 15.

#### B. Static Aeroelastic Results

To assess the grid convergence of the solutions, the static aeroelastic center-of-pressure increment has been computed at three grid levels at three transonic Mach numbers. The present analysis calculates the nondimensional aeroelastic center-of-pressure increment by

$$(\Delta c.p.)_{ae} = \left( \frac{C_m}{C_Z} \right)_{flex} - \left( \frac{C_m}{C_Z} \right)_{rig} \quad (15)$$

Results are shown in Fig. 4. Coarse, baseline, and fine grid solutions are computed at Mach 0.50, 0.90, 1.20, and 1.55. Static aeroelastic solutions are computed at an angle of attack of 2.5 deg (5 deg at Mach 0.50). These nonzero angles of attack are still within the dispersed angle-of-attack range, and they are large enough that the  $z$  force is sufficiently large to correctly compute the c.p. shift. Considering the overall features of the aeroelastic c.p. increment, it is clear that there is a large and rapidly varying influence that flexibility has on static aerodynamics in the transonic range. The major contributor to the shift in the center of pressure through the transonic range is the shifting position of the shock. The rapid positive trend in the aeroelastic center-of-pressure increment with Mach number is due to the formation of supersonic flow over the crew module. At low transonic Mach numbers, this supersonic flow is terminated by a shock near the crew module. Aft movement of the shock from the crew module to the frustum with increasing Mach number between Mach 1.2 and 1.5 is the cause of the downward trend in the aeroelastic center-of-pressure increment over a very short Mach number range. Because of shock motion, the transonic Mach number range is substantially more sensitive to grid resolution than either the subsonic or supersonic ranges. At Mach 1.20, the solution on the baseline and fine grids shows a significantly smaller shift than does the coarse grid solution. Likewise, at Mach 0.90, both the baseline and fine grids show a center-of-pressure aeroelastic increment that is smaller than the coarse solution. These results suggest that the coarse solution may overpredict the change in the center of pressure through the transonic range.

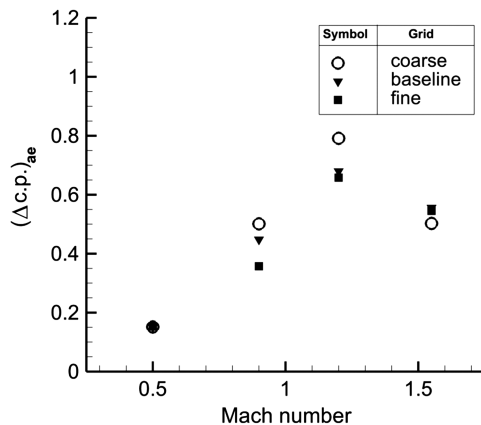


Fig. 4 Effect of grid resolution on  $(\Delta c.p.)_{ae}$ , AIIM1 model at  $q_{nom}$ .

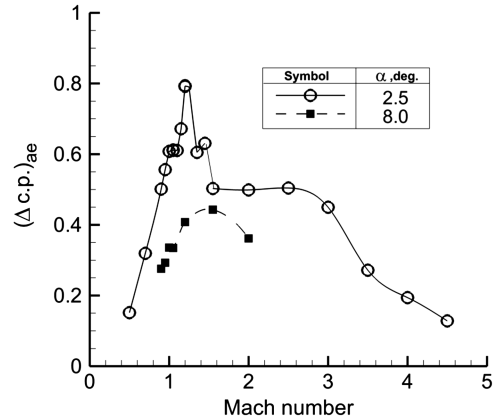


Fig. 5 Effect of angle of attack on  $(\Delta c.p.)_{ae}$ , coarse grid, AIIM1 model at  $q_{nom}$ .

The flexibility-induced center-of-pressure increments at 2.5 and 8 deg angles of attack are shown in Fig. 5. At 8 deg, the aeroelastic center-of-pressure increment is much lower than at 2.5 but still positive. These results most likely reflect the fact that shock strength and movement are less pronounced and  $z$  force is larger at the higher angles of attack than at a low angle of attack.

Figure 6 presents a comparison of the aeroelastic center-of-pressure increment due to the fully interactive CAE analysis with that due to the FRILLS solutions. FRILLS predicts the largest aeroelastic center-of-pressure increment at Mach 1.55, whereas the fully coupled aeroelastic solution puts it at Mach 1.2. The FRILLS aeroelastic center-of-pressure increment peaks at a somewhat lower value than does the CAE solution. At Mach 4.5, the solutions by the two methods are very similar, whereas at Mach 0.5, the aeroelastic center-of-pressure increment due to the FRILLS method is somewhat higher. These results indicate that the static aeroelastic solutions are most sensitive in the transonic Mach number range to grid resolution, angle of attack, and the method of simulation. It is most important to notice that the commonly used FRILLS method may in fact be nonconservative in this Mach range.

#### C. Dynamic Aeroelastic Results

Time-accurate aeroelastic analyses have been performed to assess dynamic aeroelastic stability. To provide an initial assessment of overall aeroelastic characteristics of the vehicles, coarse grid dynamic computations were performed at all analysis conditions at  $\alpha = 0$  and 2.5 deg ( $\alpha = 5$  deg at Mach 0.5), and at nominal and 1.32 times nominal dynamic pressure. The measurement of damping required excitation of a dynamic solution by an initial modal velocity. Once a solution was obtained, the log decrement method was applied to the first three or four cycles of oscillation of the modal time histories.

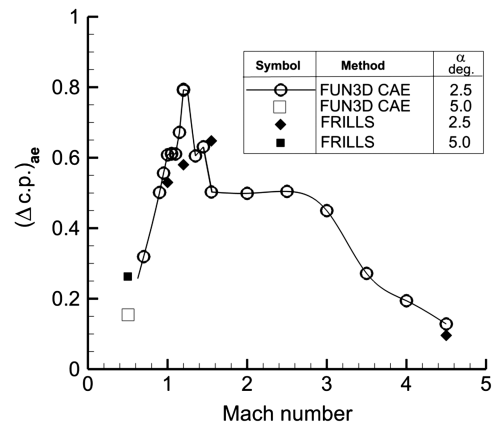


Fig. 6 Effect of solution method on  $(\Delta c.p.)_{ae}$ , coarse grid, AIIM1 model at  $q_{nom}$ .

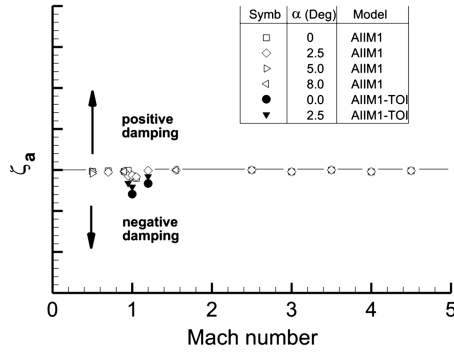


Fig. 7 Damping based on initial growth, coarse grid at  $q_{nom}$ .

Figure 7 shows the minimum modal aerodynamic damping at each trajectory condition. The figure plots the ratio of aerodynamic modal damping to critical structural damping. Typically, the least stable mode is the first mode, but at some conditions at which all modes are damped, a higher mode may prove to be the most lightly damped. At high supersonic and low subsonic Mach numbers, the magnitude of damping of the least stable mode is small. In the transonic range, there is a negative dip in damping. Significantly negative aerodynamic damping of the first mode occurs over a range from just below Mach 1.0 to around Mach 1.20. The minimum aerodynamic damping of mode 1 is at Mach 1.0.

Having identified the most critical condition to be at Mach 1.0, additional analyses are focused on understanding the behavior of the vehicle at that condition. A study of the effect of grid resolution on the aerodynamic damping was performed. Results are shown in Fig. 8. In that and remaining figures, left-hand direction represents

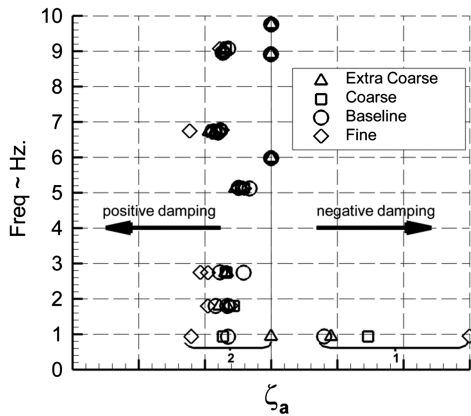


Fig. 8 Effect of grid resolution on damping, Mach 1.00,  $\alpha = 0$  deg, AIIM1-TOI model at  $q_{nom}$ .

positive aerodynamic damping while right represents negative aerodynamic damping. Time-accurate CAE solutions are computed using the coarse, baseline, and fine grids. Each solution is initiated by the same excitation of each mode. Regarding the damping values shown in Fig. 8, modes 3 and higher show very little sensitivity to grid resolution. Mode 2 damping increases with grid resolution, while mode 1 computed with the fine grid is much more undamped than with the other grids. The conclusion from this grid study is that even the fine grid does not show a sufficiently converged damping of the first mode oscillation.

Because of constraints on available computing, the remaining results were computed with the coarse grid. Figure 9 provides a comparison the damping of the fully coupled time-accurate aeroelastic solutions with the linearized FRILLS method. The condition is Mach 1.0 at nominal dynamic pressure using the coarse grid. The aerodynamic damping of modes 3 and higher are very similar between the two methods. On the other hand, the two methods produce damping values of modes 1 and 2 that are much different. The FRILLS method indicates that modes 1 and 2 are strongly damped for both the AIIM1 and the AIIM1-TOI structural models. The dynamic FUN3D solutions indicate mode 2 to be damped while mode 1 is undamped. It is also interesting to note that the AIIM1-TOI model shows a greater separation in damping of the first two modes than does the AIIM1 model, as indicated mainly by the much more negative modal aerodynamic damping in the AIIM1-TOI mode 1.

Because the amplitudes of modes 1 and 2 are nearly identical but orthogonal, it was of interest to investigate the cause of the difference in the damping of the two modes at Mach 1.0. The results of a study of the influence of OML on the dynamic aeroelastic behavior of the vehicle are shown in Figs. 10a and 10b. On the left is shown the damping of the original OML (with all protuberances) at  $q_{nom}$ , repeated from Fig. 9b, and  $1.32q_{nom}$ . Figure 10b shows the damping from a computation using a clean OML with ring protuberances only; all other protuberances were removed. The damping of modes 1 and 2 of the clean OML are nearly identical. These results indicate that the reason for the strongly damped mode 2 and undamped mode 1 is the effect that protuberances have on the vehicle aerodynamics. Apparently, an asymmetry in the locations of protuberances causes the predominantly lateral mode 2 to be damped and the predominantly longitudinal mode 1 to be undamped.

V. Conclusions

This paper discussed two areas in which CAE analyses have been performed in the support of developing the Ares I launch vehicle. The first is an understanding of the influence of flexibility on static vehicle response. The vehicle displays considerable sensitivity of center-of-pressure aeroelastic increment to grid resolution, solution method, and freestream Mach number in the transonic speed range. Between Mach 1 and the maximum dynamic pressure condition, there is a large positive center-of-pressure increment due to flexibility

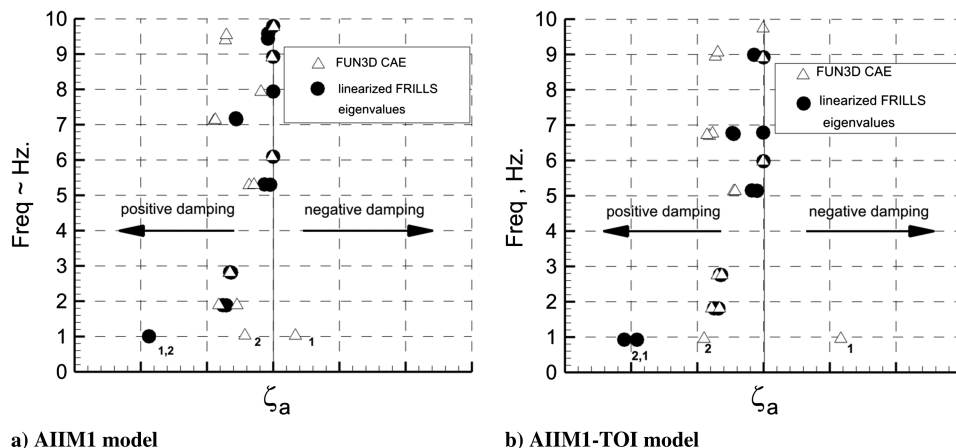
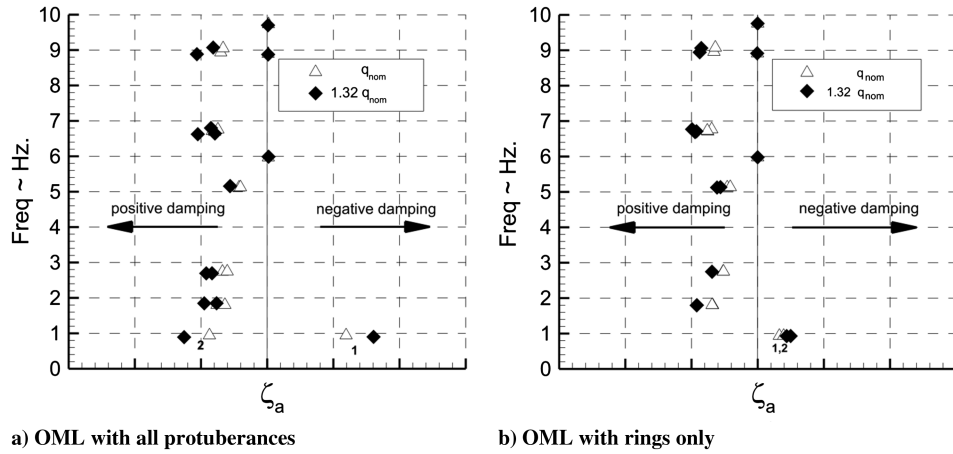


Fig. 9 Effect of structural model and solution method on damping, coarse grid, Mach 1.00,  $\alpha = 0$  deg at  $q_{nom}$ .



**Fig. 10** Effect of OML asymmetry on damping, coarse grid, Mach 1.00,  $\alpha = 0$  deg, AIIM1-TOI model.

(positive forward). Through this Mach range, there is also a large and rapid change in the aeroelastic center-of-pressure increment with increasing Mach number. A second area was an assessment of the dynamic aeroelastic stability of the launch vehicle. The modal aerodynamic damping values were computed from a log decrement of the time history of the fully coupled aeroelastic solutions. Analyses over the complete ascent trajectory have been presented, using a time-marching dynamic CFD based aeroelastic analysis. In the transonic Mach range, the modal aerodynamic damping has a negative dip. The largest negative damping is at Mach 1. The AIIM1-TOI structural model, with its added isolator springs, results in a more negative modal aerodynamic damping than the AIIM1 model. Selected conditions also were presented to compare a full aeroelastic interaction with results derived from the method of quasi-steady line loads. The modal aerodynamic damping values from a full aeroelastic interaction are compared with the eigenvalues of linearized equations derived from quasi-steady line loads. Both static and dynamic aeroelastic results show that, away from the transonic Mach range, the two methods agree reasonably well. The methods agree very well in the supersonic Mach range. In the transonic range, the dynamic aeroelastic stability results calculated using the quasi-steady method do not agree well with those due to a fully coupled aeroelastic time-marching CFD analysis. In either the static or dynamic sense, the method of quasi-steady line loads produces results that are significantly nonconservative. The present results suggest at the very least that, through the transonic Mach range, a method that provides the physically correct time-accurate fluid/structure interaction is needed to predict dynamic flexible vehicle behavior.

**Appendix**

The matrices  $[T_y]$  and  $[T_z]$  used in Eqs. (11) and (12) relate the y and z displacements to the local angles of sideslip and attack. They are defined by

$$\begin{aligned}
 [T_y] &= - \begin{bmatrix} 0 & 1 & 0 & 0 & 0 & 0 \\ & \vdots & & \ddots & & \vdots \\ 0 & 0 & 0 & 0 & 1 & 0 \\ & & & & & \\ 0 & 0 & 1 & 0 & 0 & 0 \\ & \vdots & & \ddots & & \vdots \\ 0 & 0 & 0 & 0 & 0 & 1 \end{bmatrix} \\
 [T_z] &= - \begin{bmatrix} 0 & 1 & 0 & 0 & 0 & 0 \\ & \vdots & & \ddots & & \vdots \\ 0 & 0 & 0 & 0 & 1 & 0 \\ & & & & & \\ 0 & 0 & 1 & 0 & 0 & 0 \\ & \vdots & & \ddots & & \vdots \\ 0 & 0 & 0 & 0 & 0 & 1 \end{bmatrix} \quad (A1)
 \end{aligned}$$

$[T_y]$  and  $[T_z]$  are  $N_{ll} \times 3N_{ll}$  matrices. The  $3N_{ll} \times N_{ll}$  matrix  $[\hat{S}]$  relates the y and z modal displacements to the matrices  $\partial[\hat{c}]/\partial\alpha$  and  $\partial[\hat{c}]/\partial\beta$ .  $[\hat{S}]$  is defined as

$$[\hat{S}] = \begin{bmatrix} 1 & 0 & \dots & 0 & 0 \\ 1 & 0 & \dots & 0 & 0 \\ 1 & 0 & \dots & 0 & 0 \\ 0 & 1 & \dots & 0 & 0 \\ 0 & 1 & \dots & 0 & 0 \\ 0 & 1 & \dots & 0 & 0 \\ & & \ddots & & \\ 0 & 0 & \dots & 1 & 0 \\ 0 & 0 & \dots & 1 & 0 \\ 0 & 0 & \dots & 1 & 0 \\ 0 & 0 & \dots & 0 & 1 \\ 0 & 0 & \dots & 0 & 1 \\ 0 & 0 & \dots & 0 & 1 \end{bmatrix} \quad (A2)$$

**References**

- [1] Hanson, P. W., and Doggett, R. V., "Aerodynamic Damping and Buffet Response of an Aeroelastic Model of the Saturn I Block II Launch Vehicle," NASA TN D-2713, 1965.
- [2] Doggett, R. V., and Hanson, P. W., "An Aeroelastic Model Approach for the Prediction of Buffet Bending Loads on Launch Vehicles," NASA TN D-2022, 1963.
- [3] Ericsson, L. E., and Pavish, D., "Aeroelastic Vehicle Dynamics of a Proposed Delta II 7920-10L Launch Vehicle," *Journal of Spacecraft and Rockets*, Vol. 37, No. 1, 2000, pp. 28–38. doi:10.2514/2.3546
- [4] Ericsson, L. E., "Aeroelastic Instability Caused by Slender Payloads," *Journal of Spacecraft and Rockets*, Vol. 4, No. 1, 1967, pp. 65–73. doi:10.2514/3.28811
- [5] Ericsson, L. E., "Unsteady Flow Separation Can Endanger the Structural Integrity of Aerospace Launch Vehicles," *Journal of Spacecraft and Rockets*, Vol. 38, No. 2, 2001, pp. 168–179. doi:10.2514/2.3690
- [6] Azevedo, J. L. F., "Aeroelastic Analysis of Launch Vehicles in Transonic Flight," *Journal of Spacecraft and Rockets*, Vol. 26, No. 1, 1989, pp. 14–23. doi:10.2514/3.26027
- [7] Scalabrin, L. C., Azevedo, J. L. F., Teixeira, P. R. F., and Awruch, A. M., "Three Dimensional Flow Simulations with the Finite Element Technique over a Multi-Stage Rocket," 40th AIAA Aerospace Sciences Meeting and Exhibit, AIAA Paper 2002-0408, 2002.
- [8] Bigarella, E. D. V., Basso, E., and Azevedo, J. L. F., "Multigrid Adaptive-Mesh Turbulent Simulations of Launch Vehicle Flows," 21st AIAA Applied Aerodynamics Conference, AIAA Paper 2003-4076, 2003.
- [9] Bigarella, E. D. V., and Azevedo, J. L. F., "Numerical Study of Turbulent Flows over Launch Vehicle Configurations," *Journal of Spacecraft and Rockets*, Vol. 42, No. 2, 2005, pp. 266–276. doi:10.2514/1.6889
- [10] Scalabrin, L. C., and Azevedo, J. L. F., "Finite Volume Launch Vehicle Flow Simulations on Unstructured Adaptive Meshes," 41st AIAA Aerospace Sciences Meeting and Exhibit, AIAA Paper 2003-0601,

- 2003.
- [11] Azevedo, J. L. F., "Aeroelastic Analysis of Launch Vehicles in Transonic Flight," 26th AIAA Aeroscience Meeting and Exhibit, AIAA Paper 1987-0708, 1987.
- [12] Azevedo, J. L. F., "Aeroelastic Analysis of Hammerhead Payloads," 29th AIAA Structures, Structural Dynamics and Materials Conference, AIAA Paper 1988-2307, 1988.
- [13] Hall, R. M., Holland, S. D., and Blevins, J. A., "Aerodynamic Characterization of a Modern Launch Vehicle," 49th AIAA Aerospace Sciences Meeting and Exhibit, AIAA Paper 2011-0010, 2011.
- [14] Ericsson, L. E., and Reding, J. P., "Report on Saturn I: Apollo Unsteady Aerodynamics," NASA TN LMSC-A650215 NAS 8-5338, 1964.
- [15] Hanson, P. W., and Doggett, R. V., "Wind-Tunnel Measurements of Aerodynamic Damping Derivatives of a Launch Vehicle Vibrating in Free-Free Bending Modes at Mach Numbers from 0.70 to 2.87 and Comparisons with Theory," NASA TN D-1391, 1962.
- [16] Blejwas, T. E., "Shuttle System Dynamic Loads Analysis," Martin Marietta Materials CR NAS8-30635, Baltimore, MD, 1975.
- [17] Crimi, P., "Aeroelastic Stability and Response of Flexible Tactical Weapons," 22nd AIAA Aerospace Sciences Meeting, AIAA Paper 1984-0392, 1984.
- [18] Oberholtzer, N. W., Schmidt, L. E., and Larmour, R. A., "Aeroelastic Behavior of Hypersonic Re-Entry Vehicles," 21st AIAA Aerospace Sciences Meeting, AIAA Paper 1983-0033, 1983.
- [19] Trikha, M., Mahapatra, D. R., Gopalakrishnan, S., and Pandiyan, R., "Analysis of Aeroelastic Stability of a Slender Launch Vehicle using Aerodynamic Data," 46th AIAA Aerospace Sciences Meeting, AIAA Paper 2008-0310, 2008.
- [20] "Flutter, Buzz, and Divergence," NASA Space Vehicle Design Criteria SP-8003, 1964.
- [21] Anderson, W. K., Rausch, R. D., and Bonhaus, D. L., "An Implicit Upwind Algorithm for Computing Turbulent Flows on Unstructured Grids," *Computers and Fluids*, Vol. 23, No. 1, 1994, pp. 1–22. doi:10.1016/0045-7930(94)90023-X
- [22] *FUN3D Manual*, NASA Langley Research Center, Hampton, VA, Nov. 2008, <http://fun3d.larc.nasa.gov> [retrieved 2012].
- [23] Spalart, P. R., and Allmaras, S. R., "One-Equation Turbulence Model for Aerodynamic Flows," 30th AIAA Aerospace Sciences Meeting and Exhibit, AIAA Paper 1992-0439, 1992.
- [24] Rumsey, C. L., and Thomas, J. L., "Application of FUN3D and CFL3D to the Third Workshop on CFD Uncertainty Analysis," NASA TM 2008-215537, 2008.
- [25] Nielsen, E. J., Lu, J., Park, M. A., and Darmofal, D. L., "An Exact Dual Adjoint Solution Method for Turbulent Flows on Unstructured Grids," *Computers and Fluids*, Vol. 33, No. 9, 2004, pp. 1131–1155. doi:10.1016/j.compfluid.2003.09.005
- [26] Biedron, R. T., and Thomas, J. L., "Recent Enhancements To The FUN3D Flow Solver For Moving-Mesh Applications," 47th AIAA Aerospace Sciences Meeting, AIAA Paper 2009-1360, 2009.
- [27] Nielsen, E. J., and Anderson, W. K., "Recent Improvements in Aerodynamic Design Optimization on Unstructured Meshes," *AIAA Journal*, Vol. 40, No. 6, 2002, pp. 1155–1163. doi:10.2514/2.1765
- [28] Saad, Y., and Schultz, M. H., "GMRES: A Generalized Minimum Residual Algorithm for Solving Nonsymmetric Linear Systems," *SIAM Journal on Scientific and Statistical Computing*, Vol. 7, 1986, pp. 856–869. doi:10.1137/0907058
- [29] Samareh, J. A., "Discrete Data Transfer Technique for Fluid-Structure Interaction," 18th AIAA Computational Fluid Dynamics Conference, AIAA Paper 2007-4309, 2007.
- [30] Farhat, C., Lesoinne, M., and LeTallec, P., "Load and Motion Transfer Algorithms for Fluid/Structure Interaction Problems with Non-Matching Discrete Interface: Momentum and Energy Conservation, Optimal Discretization and Application to Aeroelasticity," *Computer Methods in Applied Mechanics and Engineering*, Vol. 157, No. 1, 1998, pp. 95–114. doi:10.1016/S0045-7825(97)00216-8
- [31] Pirzadeh, S. Z., "Advanced Unstructured Grid Generation for Complex Aerodynamic Applications," 26th AIAA Applied Aerodynamics Conference, AIAA Paper 2008-7178, 2008.
- [32] Bartels, R. E., Vatsa, V., Carlson, J.-R., Park, M., and Mineck, R., "FUN3D Grid Refinement and Adaptation Studies for the Ares Launch Vehicle," 28th AIAA Applied Aerodynamics Conference, AIAA Paper 2010-4372, 2010.
- [33] Hanson, P. W., and Doggett, R. V., "Aerodynamic Damping of a 0.02-Scale Saturn SA-1 Model Vibrating in the First Free-Free Bending Mode," NASA TN D-1956, 1963.

S. P. Pao  
Associate Editor